Nanoscale Horizons

ROYAL SOCIETY OF CHEMISTRY

FOCUS

View Article Online
View Journal | View Issue

Cite this: *Nanoscale Horiz.*, 2024, 9, 2234

Crucial role of structural design on performance of cryogel-based EMI shields: an experimental review†

Sara Rostami,[a] Ahmadreza Ghaffarkhah,[ab] Seyyed Alireza Hashemi,[a] Stefan Wuttke,[cd] Orlando J. Rojas[bef] and Mohammad Arjmand*[a]

In the field of electromagnetic interference (EMI) shielding with materials based on highly porous constructs, such as foams, cryogels, aerogels and xerogels, a significant challenge lies in designing structures that primarily absorb rather than reflect incident electromagnetic waves (EMWs). This goal necessitates a dual focus on the electrical conductivity and the internal porosity of the given porous material. To explore these issues, we fabricated various graphene oxide (GO)-based cryogels by molding, emulsion templating, chemically-induced gelation, freeze-casting, and liquid-in-liquid streaming. Following thermal annealing to enhance electrical conductivity for effective EMI shielding, we assessed the physicochemical, mechanical and structural characteristics of these cryogels. Notably, the cryogels exhibited distinct EMI shielding behaviors, varying significantly in terms of primary shielding mechanisms and overall shielding effectiveness (SE_T). For example, chemically-crosslinked cryogels, which showed the highest electrical conductivity, predominantly reflected EMWs, achieving a reflectance of approximately 70% and a SE_T of 43.2 dB. In contrast, worm-like cryogels, despite having a similar SE_T of 42.9 dB, displayed a unique absorption-dominant shielding mechanism. This was attributed to their multi-scale porosities and numerous internal interfaces, which significantly enhanced their ability to absorb EMWs, reflected in an absorbance of 54.7%. Through these experiments, our aim is to provide key heuristic rules for the structural design of EMI shields.

Received 15th May 2024,
Accepted 30th September 2024

DOI: 10.1039/d4nh00210e

rsc.li/nanoscale-horizons

1. Introduction

The widespread use of wireless platforms and high-frequency devices has introduced a new generation of environmental pollution known as electromagnetic interference (EMI).[1,2] EMI is known to degrade the performance of sensitive electronics and jeopardize human health and the environment.[2–4] As our dependence on digital technologies deepens, the quest for effective EMI shielding solutions becomes a focal point in the realm of advanced materials.[2,5–9]

Metals have long been favored for EMI shielding due to their high electrical conductivity, which allows them to block the propagation of electromagnetic waves (EMWs) through the reflection.[6] However, the high reflectance of metallic shields can lead to secondary electromagnetic pollution that is as detrimental as the original waves. Furthermore, metals are heavy and susceptible to corrosion, making them unsuitable for the new generation of flexible and miniaturized electronics.[10] Given these limitations, much attention has shifted towards developing synthetic EMI shields made of carbonaceous nanomaterials,[5,6,10–12] intrinsically conductive polymers,[11,13–17] and metallic nanowires.[18,19] However, challenges such as adjusting the electrical conductivity of these materials, minimizing reflection, and mitigating secondary unwanted emissions have yet to be thoroughly addressed.[10,20,21]

To confront the limitations of traditional shields effectively, we must consider two key factors simultaneously.[22] Firstly, the electrical conductivity of designed shields should be low enough to permit a significant portion of EMWs to enter with minimal reflectance.[23,24] This point is best illustrated by thin films of highly conductive materials like MXenes and graphene.

[a] *Nanomaterials and Polymer Nanocomposites Laboratory, School of Engineering, University of British Columbia, Kelowna, BC, V1V 1V7, Canada. E-mail: mohammad.arjmand@ubc.ca*
[b] *Bioproducts Institute, Department of Chemical & Biological Engineering, The University of British Columbia, 2360 East Mall, Vancouver, BC, V6T 1Z3, Canada*
[c] *Basque Centre for Materials, Applications & Nanostructures (BCMaterials), Bld. Martina Casiano, 3rd. Floor UPV/EHU Science Park Barrio Sarriena s/n, Leioa, 48940, Spain*
[d] *IKERBASQUE, Basque Foundation for Science, Bilbao, 48013, Spain*
[e] *Department of Chemistry, The University of British Columbia, 2036 Main Mall Vancouver, Vancouver, BC, V6T 1Z1, Canada*
[f] *Department of Wood Science, The University of British Columbia, 2900-2424 Main Mall, Vancouver, BC, V6T 1Z4, Canada*

† Electronic supplementary information (ESI) available. See DOI: https://doi.org/10.1039/d4nh00210e

While these materials have been hailed as revolutionary in EMI shielding due to their high conductivity, thin films of these materials exhibit a reflectance comparable to metal-based shields. Consequently, these thin films are not optimal for absorption-dominant shields as they hinder the penetration of incident waves, limiting absorption capacity significantly.[24,25]

Secondly, developed shields should effectively attenuate the energy of waves that penetrate the structure. In this regard, in addition to material selection, the structural design of EMI shields is crucial.[21,26,27] For instance, developing porous constructs of conductive materials such as graphene and MXene offers a potential solution for achieving absorption-dominant characteristics. Within highly porous structures, *i.e.*, foams, cryogels, aerogels, and xerogels, the concept of multiple internal reflections or internal scattering plays a crucial role by prolonging the interaction of EMWs with the material. This extended interaction significantly enhances the porous constructs' ability to absorb EMWs, thereby improving their overall shielding effectiveness.[28–31] All in all, for designing absorption-dominant EMI shields, also known as electromagnetic traps or green shields, maintaining moderate electrical conductivity throughout the structure is essential. While this concept is theoretically straightforward, implementing such a structural design remains an underexplored area in the field of EMI shielding, indicating a need for more attention and research focus.

So far, the focus on the structural design of EMI shielding materials based on porous structures has predominantly centered on conductive cryogels and cryogels based on 2D nanomaterials like MXenes, graphene, and reduced graphene oxide (rGO).[32] Among these, graphene-based systems derived from graphene oxide (GO) and subjected to thermal or chemical reduction for enhanced electrical conductivity stand out due to their chemical stability, ease of aqueous fabrication, and acceptable mechanical properties.[33,34] Various fabrication methods such as freeze-casting,[35–37] emulsion templating,[38,39] chemically-induced gelation,[33,40,41] and liquid streaming assembly[7,10,42] have been employed to produce GO-based porous, each yielding distinct internal characteristics, porosities, mechanical performance, and chemical properties.[34] For instance, freeze-cast cryogels are notable for their aligned pores with temperature gradients,[35] while liquid-templated worm-like cryogels are favored for their macro-to-micro-scale porosity.[34] Despite numerous studies designing these cryogels using different methods for EMI shielding applications, the impact of internal structure on the EMI shielding properties of cryogels produced *via* diverse methods remains to be fully understood.

Herein, we explore how cryogel fabrication impacts the structural characteristics, mechanical properties, and EMI shielding performance of GO-based cryogels. Using GO as the primary building material, we created cryogels through various techniques, including molding, emulsion templating, unidirectional freeze-casting, chemically-induced gelation, and liquid streaming. After subjecting them to thermal annealing to achieve the desired electrical conductivity, we assessed their internal porosity, mechanical properties, and chemical attributes. This analysis highlights the potential of fabrication methods, particularly the liquid streaming that yields worm-like cryogels, to develop next-generation absorption-dominant EMI shields. It showcases pronounced absorption-dominant characteristics and substantial shielding effectiveness, suggesting a promising direction for advancing EMI shielding technology. On the other hand, cryogels produced through methods like chemically-induced gelation might not significantly outperform traditional EMI shields. These cryogels typically exhibit reflection-dominant characteristics and lower shielding effectiveness. These findings provide crucial guidelines for advancing green EMI shielding technologies, underscoring the essential interplay between electrical conductivity and internal structure. This interplay is vital for designing effective absorption-dominant EMI shields.

2. Results and discussion

2.1. From graphene oxide aqueous suspension to porous cryogels

The characterization of the synthesized GO flakes used in the developed cryogels is summarized in Section 1 and Fig. S1, S2 (ESI†). However, when these flakes are used for cryogel fabrication, the alignment, pore distribution, internal surface area, and overall structural stability of the resulting cryogels are highly dependent on the chosen fabrication strategies, such as direct molding, emulsion templating, chemically-induced gelation, unidirectional freeze-casting, and liquid streaming.[43,44] Among these methods, the direct molding approach involves pouring GO suspensions into a mold without any pre-processing, followed by a freezing/lyophilization process.[45] In this approach, pore distribution is influenced by random ice crystals formation during freezing, which is then preserved through sublimation (Fig. 1(a)). As shown in Fig. 1(b)-I–III and Fig. S3a–e (ESI†), the as-fabricated cryogels exhibit micro-scale pores with an average size of 76.8 ± 34.4 μm with random arrangements, with no evident alignment in any specific direction was observed for the generated pores (Fig. S3f, g, ESI†).

To modify the physio-mechanical characteristics of porous structures, emulsion templating was introduced into the cryogel fabrication process. This approach minimizes the density of the cryogels, enhancing their functional properties for various applications.[46] In our approach, we used an oil-in-water Pickering emulsion containing an aqueous phase of GO as the major phase and hexane/PSS-[3-(2-aminoethyl)amino]propyl-heptaisobutyl substituted POSS (POSS–NH_2) as a dispersed phase, serving as a template for fabricating lightweight cryogels. The formation of these cryogels relies on both the chemical characteristic of the GO flakes and the presence of an interfacial active ligand, *i.e.*, POSS–NH_2.[7,10]

GO exhibits dual hydrophobic/hydrophilic characteristics, with a hydrophobic basal plane and hydrophilic functional groups such as hydroxyl, carboxyl, and epoxide groups. Consequently, GO nanosheets tend to migrate toward the hexane/water interface, reducing interfacial tension by acting as a surfactant. At the hexane/water interface, the interaction between deprotonated carboxylic functional groups of GO and protonated amine groups of POSS–NH_2 generates nanoparticle

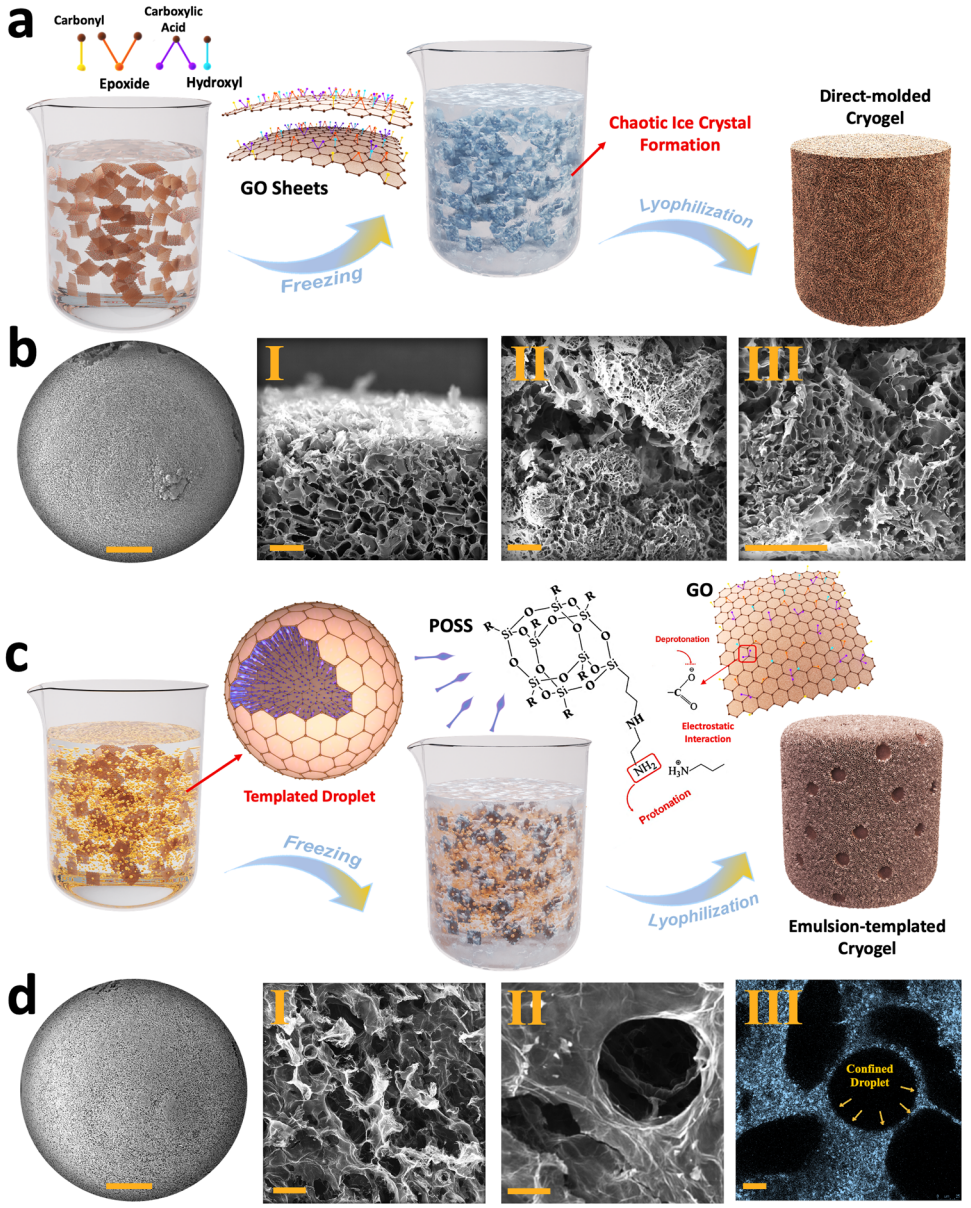

Fig. 1 (a) Schematic illustration of direct molding fabrication approach, in which cryogels were formed through molding, freezing, and lyophilization. (b) Top view and (b-I) side view of the molded cryogel: (b-II–III) FESEM images showcase chaotic pore size and distribution with no apparent alignment in any direction. (c) Schematic illustration of emulsion templating method. Structured Pickering emulsions were prepared using a 60 : 40 vol% ratio of ~10 mg ml^{-1} GO suspension and a mixture of 1 mg ml^{-1} hexane/POSS–NH_2. The emulsion-templated cryogels with secondary porosity were created after subsequent freezing and freeze-drying of the structured Pickering emulsion. (d) Top view and (d-I–II) FESEM images of emulsion-templated cryogels. (d-III) Confocal images of oil-in-water Pickering emulsion leading to the confinement of the non-polar droplets in GO aqueous suspension. The colored phase showcases the presence of aqueous GO, while black circles represent the oil droplets containing ligands. Scale bars in (b), (d), (b-I–III and d-I–II), and (d-III) correspond to 2 mm, 200 μm, and 25 μm, respectively.

surfactants at the liquid–liquid interface that upon jamming form structured Pickering emulsions (Fig. 1(c)). Upon freeze-drying, two distinct types of porosities are observed within the resulting cryogels (Fig. 1(d)-I, II and Fig. S4, ESI†). Similar to direct-molded cryogels, micro-scale pores appear inside the cryogels due to ice crystal formation in the aqueous phase, with an average size of 48.2 ± 13.6 μm. Additionally, confined hexane droplets leave numerous voids inside the structure after drying, creating what we refer to as porosity type II, with an average size of 142.8 ± 32 μm (Fig. 1(d)-III and Fig. S5, ESI†).

Chemically-induced gelation of GO is among the methods routinely employed as a pre-processing step for cryogel fabrication scenarios.[34,47] In this approach, ethylenediamine (EDA) was added to GO suspension to assemble nanosheets into a 3D monolithic graphene hydrogel (Fig. 2(a)). In this chemical reaction, the carboxyl, hydroxyl, and, in some cases, the epoxide functional groups present on GO react with the amine groups of

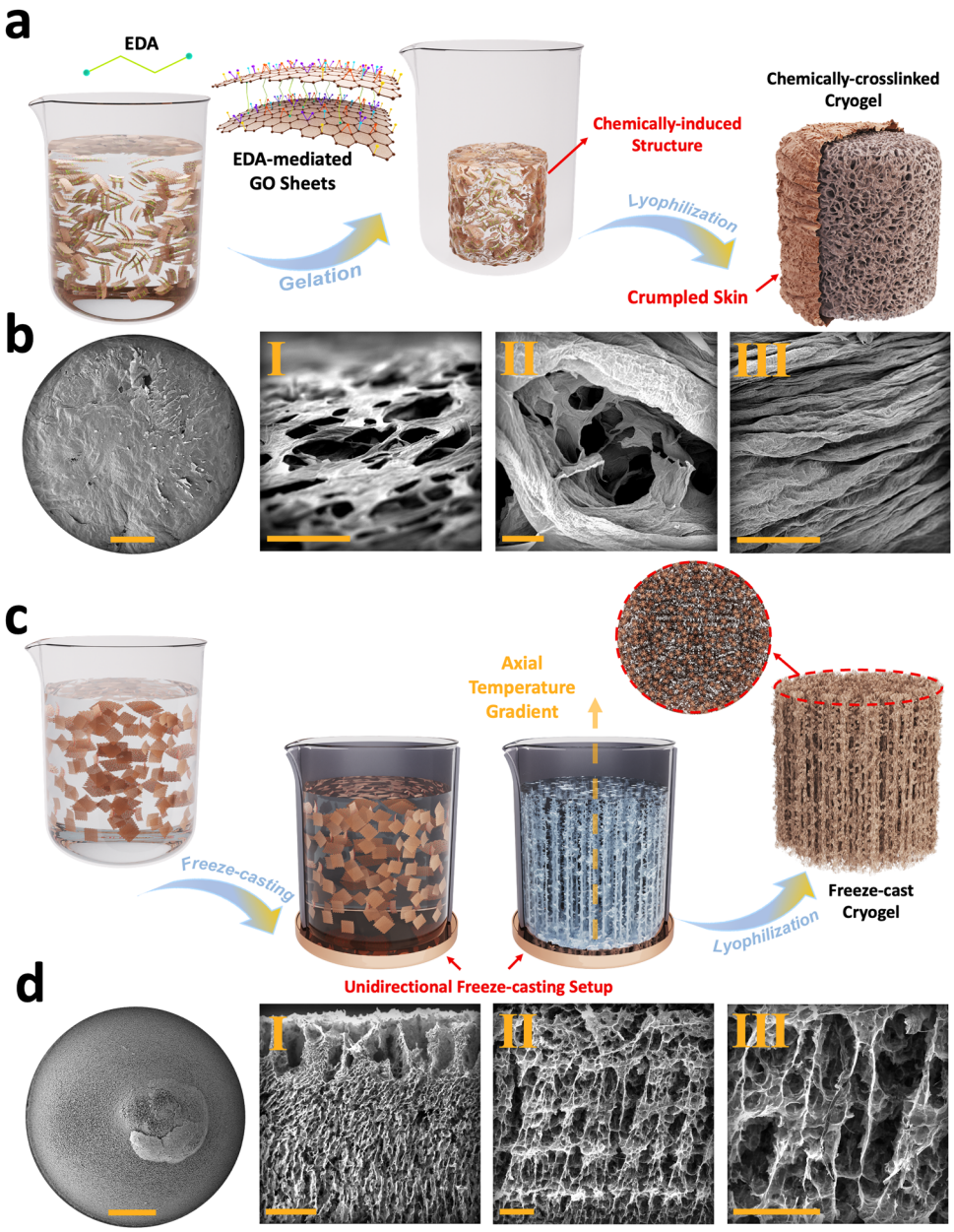

Fig. 2 (a) Schematic illustration of chemically-crosslinked cryogels. During gelation, the gel's network entraps solvent molecules and forms a cohesive structure-intact hydrogel, where the initial volume shrinkage is visualized. As the hydrogel undergoes drying, the structure shrinks for the second time due to capillary forces and surface tension. These shrinkages can lead to the formation of wrinkles, folds, or crumples on the surface of the gel. (b) Top view and (b-I–III) FESEM images of chemically-crosslinked cryogels, demonstrating (b-I and b-II) the foam-like interconnected core wrapped with (b-III) folded and crumpled skin. (c) Schematic illustration of unidirectional freeze-casting mechanism and the resulting cryogel. (d) The top view and (d-I–III) longitudinal section of the freeze-cast cryogel reveal that ice crystal nucleation from bottom to top leads to elongated pore alignment. Scale bars in (b and d), (b-I, b-III, d-I–III) and (b-II) correspond to 2 mm, 200 μm and 50 μm, respectively.

EDA (Fig. S6, ESI†).[33] This interaction reduces and cross-links GO nanosheets and, subsequently, forms graphene hydrogels. These functionalized graphene hydrogels are then subjected to successive freezing/lyophilization to form chemically-crosslinked graphene cryogels.[33] FESEM images of these cryogels exhibit foam-like structures with crumpled skin (Fig. S7a–c, ESI†), enveloping a 3D interconnected core (Fig. 2(b)-I–III) with micro-scale porosity, having an average size of 75.5 ± 19.8 μm (Fig. S7d–h, ESI†). The cell walls are formed through EDA-mediated assembly of GO sheets, in which individual flakes are pressed together and subsequently densified during the freezing process.

Unidirectional freeze-casting is another method commonly used in the fabrication of graphene cryogels. In this technique, the alignment and distribution of 2D nanoflakes are controlled through bottom-up nucleation and growth of ice crystals (Fig. 2(c)).[47] To achieve this, we used a polymeric mold featuring a copper bottom. When an aqueous suspension of GO is

poured into a mold and exposed to liquid nitrogen, ice crystals begin to form from the bottom and propagate upwards in the out-of-plane direction.[36,37] The formed vertically aligned ice crystals push the suspended flakes to the sides, leading to the 3D alignment of GO sheets. After lyophilization, the ice crystals are removed, leaving behind longitudinal micro-scale pores with an average size of 174.6 ± 56.5 μm (Fig. S8a–e, ESI†) and transverse micro-scale pores with an average size of 68.8 ± 19.5 μm (Fig. S8f–j, ESI†), which replicate the extended ice crystals/templates formed during freezing (Fig. 2(d)-I–III).

On the other hand, liquid-in-liquid streaming of GO aqueous suspension into a non-polar domain containing a ligand has been reported to produce worm-like liquid templates (Fig. S9a, ESI†). This method is promising for developing ultra-lightweight graphene cryogels with multi-scale porosity.[10,34,42] Similar to the emulsion templating approach, liquid streaming

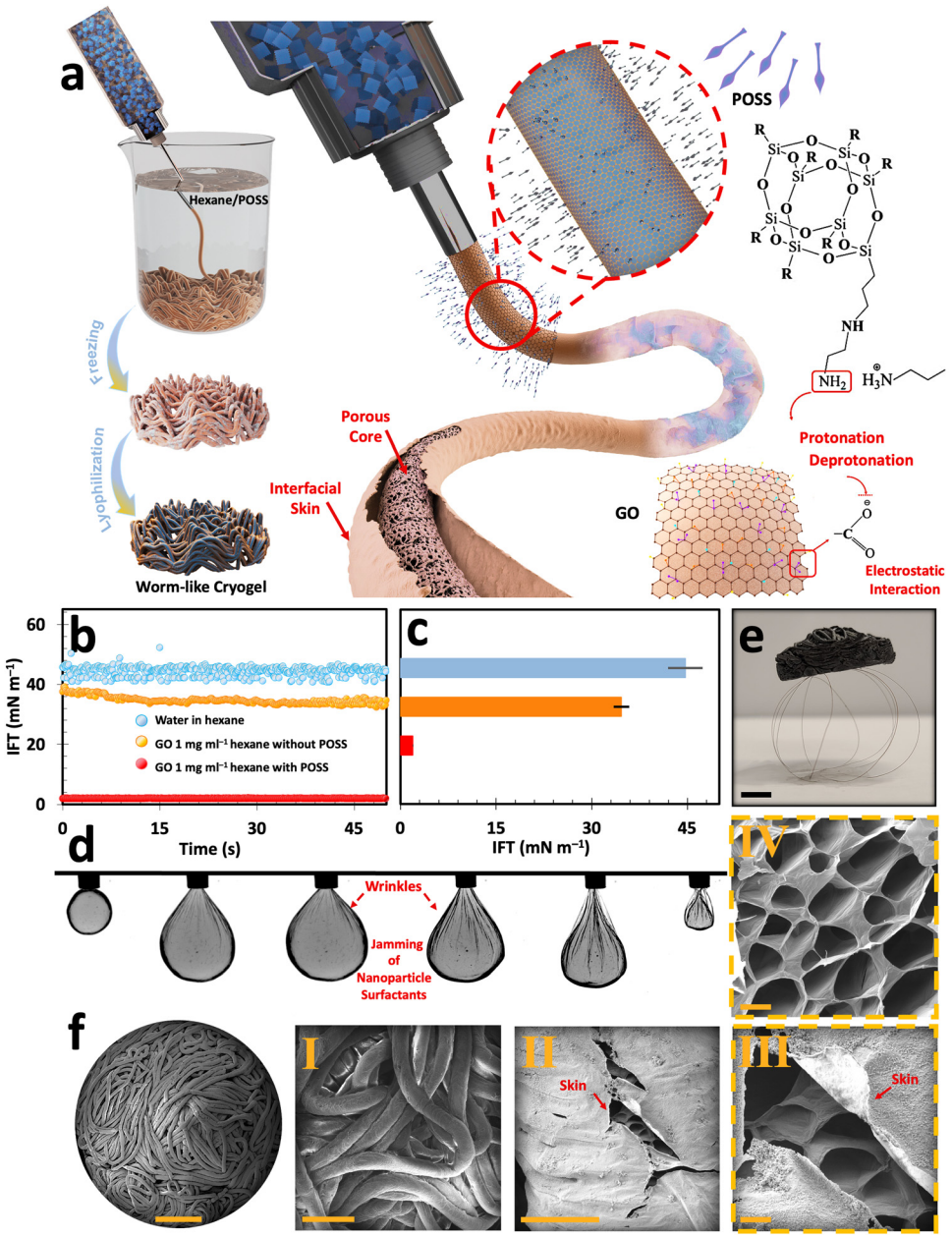

Fig. 3 (a) Schematic illustration of liquid filaments formation upon injecting GO aqueous suspension in hexane/POSS–NH_2 medium and the resulting worm-like cryogel. (b) A comparison of IFT values of water and 1 mg ml^{-1} GO droplet in the hexane domain with/without POSS–NH_2 and (c) their average values over 50 seconds. (d) Expansion/contraction analysis of 1 mg ml^{-1} GO aqueous ink within the hexane/POSS–NH_2 domain. Wrinkles on the droplets prove the nanoparticle surfactant assembly and jamming on the interface. (e) Digital image of ultra-flyweight worm-like cryogels after thermal reduction on a few human hairs. (f) The corresponding FESEM images showcase dual (f-I) macro-scale voids between the filaments and (f-II–IV) micro-scale porosity within the as-fabricated robust skin. Scale bars in (e), (f, f-I), (f-II), and (f-III–IV) correspond to 10 mm, 2 mm, 200 μm, and 20 μm, respectively. All error bars in (c) represent the standard deviation.

relies on interfacial assembly and jamming of nanoparticle surfactants, *i.e.*, GO/POSS–NH_2 (Fig. 3(a)).[48] Upon introducing a falling stream of GO aqueous suspension into the hexane/POSS–NH_2 domain, the ligand molecules promptly migrate to the interface, effectively reversing the previous negative charge of the water/hexane interface into a positive one. The GO flakes then migrate to the interface, where their carboxylic functional groups get deprotonated and form electrostatic bonds with the positively charged protonated groups of POSS ($-NH_3^+$). This electrostatic interaction forms GO/POSS–NH_2 nanoparticle surfactants that, upon jamming, stabilize a falling stream of aqueous GO suspension and suppress Plateau–Rayleigh instabilities.[48]

To further investigate the assembly and jamming of nanoparticles at the liquid–liquid interface, the dynamic interfacial tension (IFT) measurements were conducted using a pendant drop tensiometer (Fig. 3(b) and (c)). Upon introducing an aqueous suspension containing 1 mg ml^{-1} GO into the non-polar hexane domain, there was a drop in IFT from $\approx$45 mN m^{-1} (typical of neat water and hexane) to 34.66 mN m^{-1}. This reduction of IFT can be explained by the surfactant-like behavior of GO, even at low concentrations, arising from its dual hydrophobic/hydrophilic nature. It is worth noting that despite its pronounced interfacial activity, pure GO aqueous suspensions fail to form stable filaments within the non-polar domain in the absence of ligands.[10,42,49] However, introducing GO suspension with the same concentration into the hexane/POSS–NH_2 medium enables the swift formation of GO/POSS–NH_2 nanoparticle surfactants. The interfacial jamming of these particles significantly reduces the IFT to 1.96 mN m^{-1}. This significantly lower IFT can be explained by the formation of a solid-like skin at the liquid–liquid interface, which stabilizes highly non-equilibrium structured liquids (Fig. S9b, ESI†).

The pulsating tests conducted by a pendant drop setup further prove the nanoparticle surfactants jamming phenomenon at the interface (Fig. 3(d)). In this test, a 1 mg ml^{-1} GO droplet is suspended within hexane/POSS–NH_2. As the droplet undergoes contraction, its volume shrinks, applying compression forces and wrinkling the interface. As reported previously, the formation of these permanent wrinkles is a sign of the strong bonding of nanoparticle surfactants at the liquid–liquid interface, which can be explained by the formation of a solid-like skin that structures a pendant drop.[48,50–54]

After subsequent freezing and freeze-drying, the filamentous liquid templates transform into worm-like cryogels (Fig. S9c, ESI†). After undergoing a post-processing thermal reduction at 800 °C under argon for 1 h, these constructs transform into electrically conductive cryogels that are lighter than their non-reduced counterparts. The ultra-lightweight nature of these cryogels is showcased in Fig. 3(e), where a reduced worm-like cryogel with an approximate volume of 15 cm^3 can stand at the top of a few human hairs. The morphological assessment of GO-based worm-like cryogels with abundant macro-to-micro-scale porosities (from 0.586 ± 0.3 mm to 18.6 ± 6.6 μm) is presented in the FESEM images of the corresponding cryogels (Fig. 3(f) and Fig. S10, ESI†). The macro-scale porosities arise from the liquid streaming process, creating numerous voids between the interlaced filaments (Fig. 3(f)-I and Fig. S11a, b, ESI†). Furthermore, the interfacially driven skin, identified as a key parameter for stabilizing the liquid streams, was clearly preserved after lyophilization as a laminated layer that envelops and covers the microporous core of the developed filaments (Fig. 3(f)-II, III and Fig. S11c–g, ESI†). These internal micro-scale porosities, akin to those found in other freeze-dried cryogels, were initiated by ice crystal formation within the filaments during freezing and subsequently locked in place upon sublimation (Fig. 3(f)-IV and Fig. S11h, i, ESI†).

2.2. Structural characteristics of GO-based cryogels

In order to achieve electrically conductive cryogels, all constructs described in previous sections underwent thermal reduction at 800 °C under argon for 1 h. X-ray diffractograms of these cryogels before and after thermal treatment are displayed in Fig. S12 and S13 (ESI†), respectively. Owing to the cryogel's uneven surface and numerous porosities, the parallel beam technique based on a polycapillary optic was employed to collect the X-ray diffraction (XRD) for cryogels.[42] Before thermal treatment, for all fabricated constructs except the chemically-crosslinked cryogel, the main fingerprint peak of GO is evident at around 2θ of 11.51°–11.76°, related to *d*-spacing values of 7.68–7.52 Å.[55–57] In the case of chemically-crosslinked cryogels, a slight peak appears in the XRD pattern at $2\theta \sim 22.78°$ with a *d*-spacing of 3.90 Å, indicating a smaller interplanar spacing compared to the other cryogels due to primary chemical reduction. Nevertheless, the *d*-spacing formed in the chemically-crosslinked cryogel before thermal treatment is still slightly larger than that of the same sample after thermal treatment. Therefore, it can be concluded that while chemically-crosslinked cryogels undergo initial or partial reduction, thermal treatment can further decrease the density of oxygen-containing functional groups in these cryogels.

Likewise, after thermal annealing of direct-molded, emulsion-templated, freeze-cast, and worm-like cryogels, 2θ value of ~26.21°–26.51°, corresponding to a *d*-spacing of ~3.40–3.36 Å, was observed for these constructs, showcasing their chemical reduction and removal of oxygen-based functional groups (Fig. S13, ESI†). The achieved *d*-spacing in reduced cryogels matches the interlayer spacing of graphite flakes, further signifying the graphitization of the stacked GO sheets by eliminating oxygen-based functional groups.[57,58]

All fabricated cryogels were analyzed *via* micro-Raman spectroscopy before and after thermal treatment to explore the rise in structural defects. Micro Raman spectroscopy identifies the defects of graphene derivatives or their cryogels due to sensitivity to phonon modes, providing valuable information regarding structural/chemical defects. Accordingly, two well-defined peaks are observed in the Raman spectra of GO-based cryogels, namely the D-band and the G-band. The D-band is attributed to the formed disorders within the graphene. Meanwhile, the G-band arises from the vibration of well-ordered sp^2-bonded carbon atoms within the graphene lattice, reflecting the graphitic nature of graphene flakes.

The I_D/I_G ratio scales with the rise in the level of the defects (level of defective sites *versus* well-ordered sp^2 carbon atoms).[59]

As illustrated in Fig. S14 and S15 (ESI†), all samples showcased two nominal peaks within the range of 1324.5–1357 cm^{-1} and 1583–1597 cm^{-1}, corresponding to the D- and G-bands of the GO or their reduced forms, respectively. In this case, the cryogel processing significantly affected the I_D/I_G ratio, which serves as an indicator of defect levels. The lowest defect level before thermal annealing was observed in the emulsion-templated cryogels, while the highest was recorded in the chemically-crosslinked cryogels. After thermal treatment, the I_D/I_G ratio increased to values at or above unity across all samples. This increase signals successful thermal reduction and the removal of oxygen-containing functional groups, consistent with findings from previous studies.[59,60]

2.3. Physical and mechanical properties of the cryogels

The physical and mechanical properties of the fabricated cryogels are crucial to justify their use in environments where these constructs are routinely subjected to various external forces. In Fig. 4(a) and (b), the density and volume shrinkage of the produced cryogels due to thermal annealing is presented. Before thermal treatment, these cryogels exhibit a density range of 4.80–10.63 mg cm^{-3}. However, after thermal annealing, this range declines to 2.47–4.54 mg cm^{-3} with an average volume shrinkage of 13.6–63.5%. Before thermal treatment, cryogels experience initial volume shrinkage due to capillary forces during the lyophilization stage.[61,62] Thermal annealing induces further structural rearrangement, where at elevated temperatures, the particles or alignments within the cryogel constructs can shift and reorganize into a more stable configuration. This often results in pore volume reduction and causes additional shrinkage, featuring a denser packing. Furthermore, during annealing, expansion followed by contraction can cause permanent structural changes in cryogels, *i.e.*, reduction in pore volume and alterations in pore size distribution.[63,64]

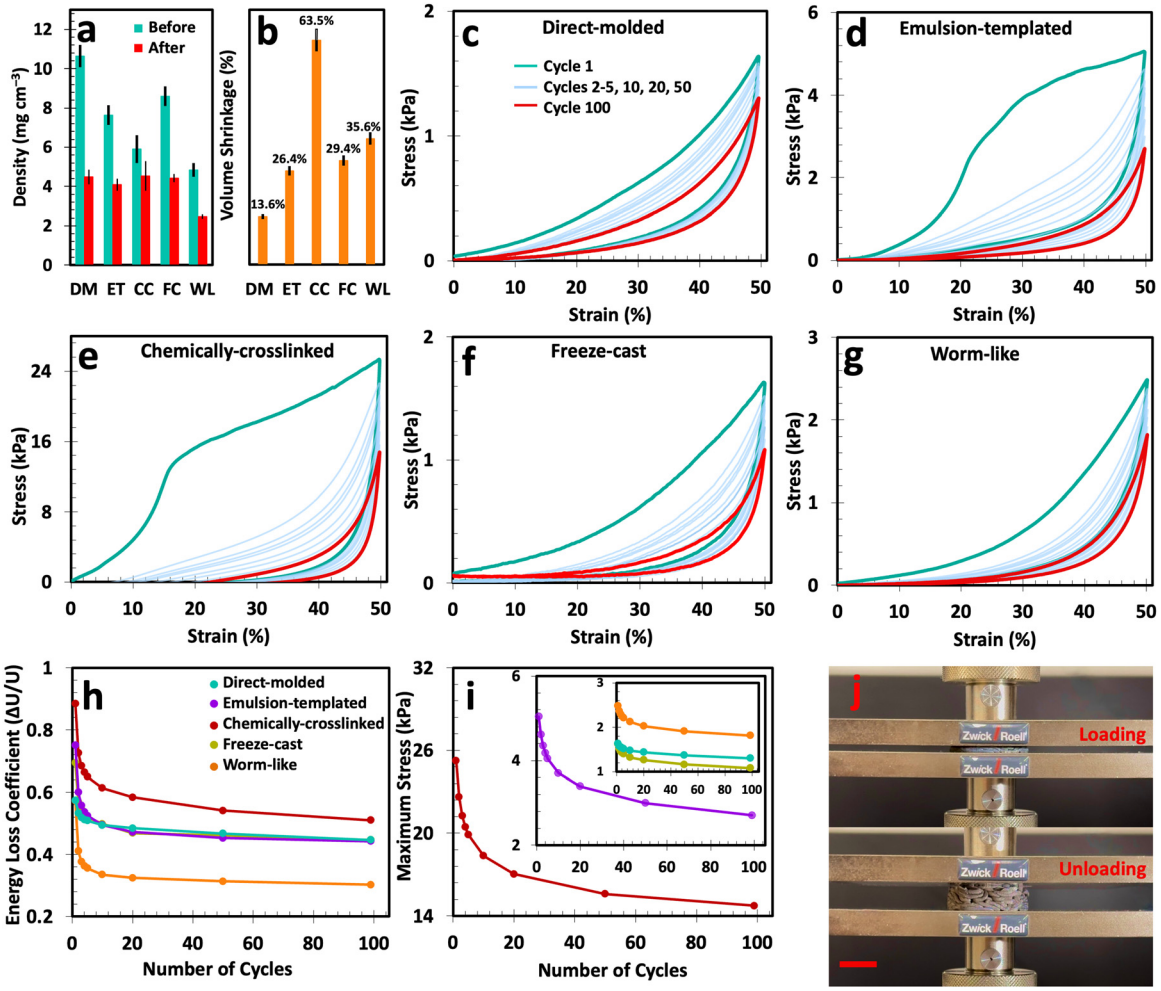

Fig. 4 (a) A comparison of the density of GO-based cryogels employing various fabrication methods before and after thermal reduction. (b) The volume shrinkage percentage of cryogels after thermal reduction. (c)–(j) Mechanical performance of cryogels: fatigue hysteresis test of (c) direct-molded (d) emulsion-templated (e) chemically-crosslinked (f) unidirectional freeze-cast (g) worm-like cryogels. The samples were compressed up to 50% strain for 100 cycles. The corresponding (h) energy loss coefficient and (i) maximum stress over repeated cycles for 50% strain. (j) Digital images of non-reduced worm-like cryogels under loading/unloading compression test. The scale bar in (j) corresponds to 10 mm. All error bars in (a) and (b) represent the standard deviation. The abbreviations DM, ET, CC, FC, and WL correspond to direct-molded, emulsion-templated, chemically-crosslinked, unidirectional freeze-cast, and worm-like cryogels, respectively.

Thermal treatment also leads to sintering, causing changes in surface chemistry—such as the reduction of oxygen-containing functional groups in GO—and resulting in the fusion of cryogels particles at junction points. Amongst all, worm-like cryogels emerge as the frontrunner in lightweight structures with an ultra-low density of 2.47 mg cm^{-3}, even by utilizing a 10 mg ml^{-1} GO suspension.[34,42] This low density is attributed to the unique morphology of worm-like cryogels—macro-scale porosity between the entangled filaments and micro-scale porosity within the tubular structures.

To assess their mechanical characteristics, all fabricated cryogels were subjected to a cyclic compression test at 20, 40, 60, 70, and 80% of compressive strains (Fig. S16, ESI†). In addition, 100 compressive cycles with a maximum strain of 50% were performed for all cryogel types. The corresponding stress–strain curves are illustrated in Fig. 4(c)–(g) and Fig. S17a (ESI†). Analysis of the unloading curves indicates that each compression results in some degree of permanent residual deformation in cryogels.[65] For all cryogel types, the initial compression cycle differs from subsequent ones. In fact, the first cycle showcases the highest Young's modulus, maximum stress, and energy loss coefficient, which clearly declined for the rest of the cycles (Fig. S17b, ESI† and Fig. 4(h) and (i)).

The fatigue hysteresis test combined with the calculated energy loss coefficient offers further insights into the mechanical stability of the samples. In brief, the energy loss coefficient shows how much energy is lost during each compression/decompression cycle. In this scenario, a lower energy loss coefficient suggests that cryogels retain more energy during cyclic loading, indicating better mechanical stability and potential for repeated use without significant performance decline. It is noteworthy that all cryogels experienced a rapid decline in energy loss coefficient within their 20 initial cycles. This decline is followed by a plateau trend, primarily due to the collapse of vulnerable pores or reconfiguration of cell walls. As a result, we have the highest energy loss coefficient factor for the first few cycles, which means there are still mechanically vulnerable pores inside the structures. However, upon reaching the plateau region, all cryogels reached their stable condition, where the remaining pores can retain more energy during compression and release it upon unloading without any further significant structural degradation.

Among all the prepared samples, worm-like cryogels represent the highest reduction in energy loss coefficient and the lowest energy loss coefficient in the plateau region. This can be explained by the unique morphology of these cryogels, where external compression forces displace the loosely attached worm-like filaments, leading to a more ordered state where filaments cannot slide atop each other.[7,10,42]

Aside from the energy loss coefficient, analyzing the highest stress value (at 50% strain) in each loading/unloading step provides us with crucial insights into the mechanical integrity of each sample. Of note, the maximum stress represents the peak amount of stress required to compress a sample to a specific strain value. Fig. 4(i) illustrates the maximum stress for the fabricated cryogels subjected to 100 compressive cycles at a maximum strain of 50%. For all cryogel types, the maximum stress has the highest value in the first cycle. However, as some pores collapse during subsequent compression cycles, the maximum stress gradually diminishes until we reach a plateau—a trend also observed in the energy loss coefficient. Such a reduction in maximum stress value is particularly evident in the chemically-crosslinked and emulsion-templated cryogels. On the other hand, the decrease in maximum stress for worm-like, direct-molded, and unidirectional freeze-cast cryogels is relatively lower compared to the samples mentioned above, indicating that the collapse of vulnerable pores has minimal impact on the maximum stress for these cryogels.

The maximum stress value not only indicates the collapse of vulnerable pores but also demonstrates each sample's ability to withstand external forces. In other words, it shows which sample requires more compressive force to achieve a specific strain. This indirectly offers significant insights into the internal structure of various cryogels. In this context, chemically-crosslinked cryogels exhibited the highest maximum stress value among the various types, even after a steep decline over $\sim$20 cycles. This structural integrity stems from the presence of cross-linkers and the formation of crumpled skin during gelation and lyophilization in chemically-crosslinked cryogels.[33,66]

2.4. EMI shielding of GO-based cryogels

As mentioned before, to prepare conductive cryogel-based EMI shields, the fabricated structures were subjected to thermal treatment at 800 °C. The electrical conductivity of thermally reduced samples is demonstrated in Fig. 5(a). Chemically-crosslinked cryogels exhibit the highest electrical conductivity of $\sim$137.3 S m^{-1} among all cryogel types. This superior electrical conductivity arises from the densely packed GO flakes formed during EDA-mediated assembly, the creation of a wrinkled skin during chemically-induced gelation, and significant volume shrinkage after thermal annealing (Fig. S18, ESI†).[65] This high electrical conductivity and the ability to withstand successive compressive cycles are desirable for the long-term use of these cryogels in sensors, wearable electronics, and flexible conductive materials.

Freeze-cast cryogels secured second place in terms of electrical conductivity owing to their prolonged porous morphology, engineered cell wall alignment, and improved electron mobility.[35] On the other hand, worm-like, emulsion-templated, and molded cryogels showcased a lower electrical conductivity range of 8.6–11.3 S m^{-1}. It is important to note that the variation in electrical conductivity among different samples is one of the factors influencing the electromagnetic interference (EMI) shielding properties of these cryogels, as will be discussed in the subsequent sections.

The EMI shielding properties of the cryogels were evaluated using a vector network analyzer (VNA). As described in ESI,† the scattering parameters (S_{ij}) were analyzed and then converted into power coefficients: transmittance ($T = |S_{12}|^2 = |S_{21}|^2$), reflectance ($R = |S_{22}|^2 = |S_{11}|^2$), and absorbance ($A = 1 - R - T$).[67] These coefficients provide crucial insights into the proportion of incident waves reflected, absorbed, and transmitted through

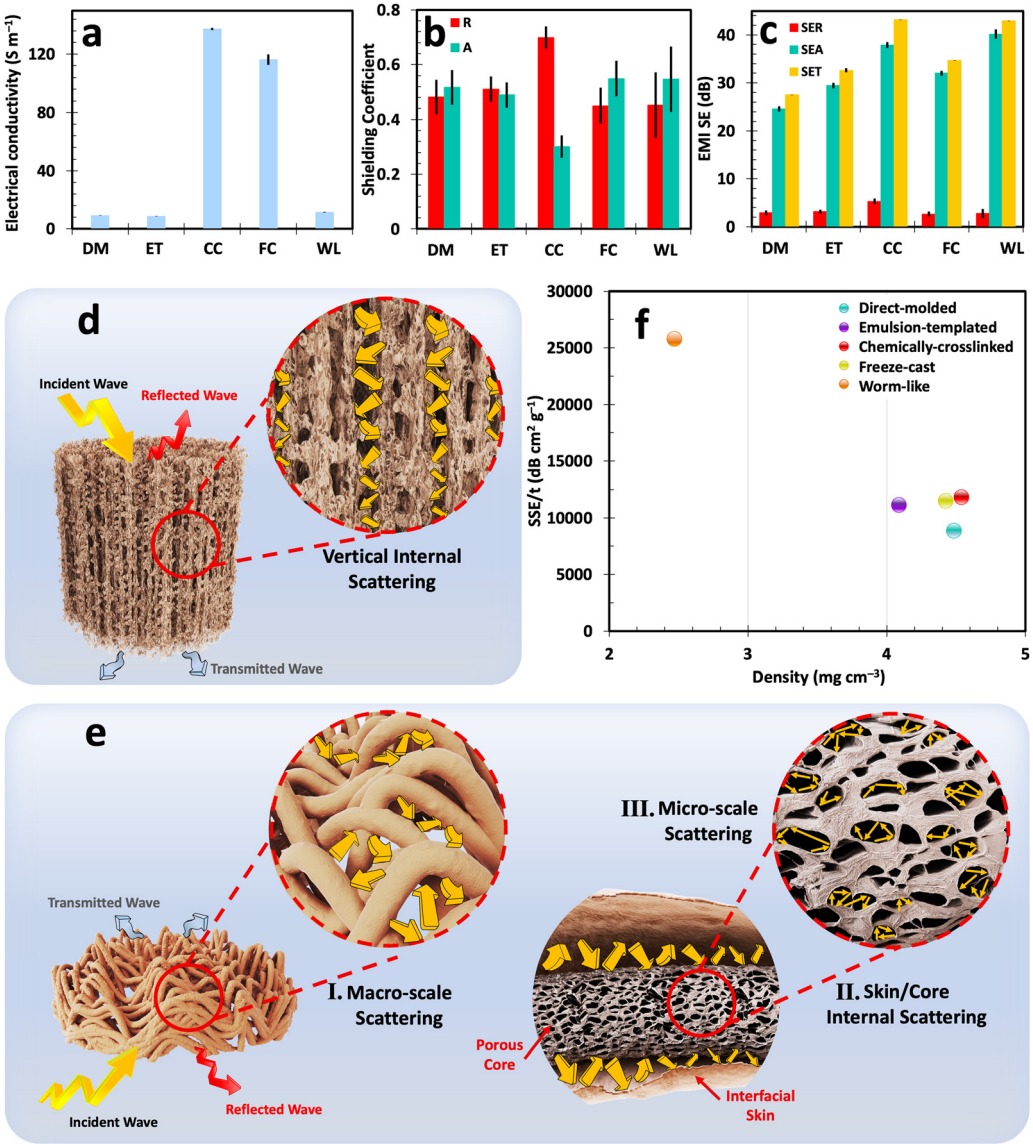

Fig. 5 (a) Electrical conductivity of the prepared cryogels through various fabrication methods after thermal annealing. (b) and (c) EMI shielding characteristics of the corresponding cryogels. (d) and (e) Schematic illustration of multiple internal reflections: (d) along the vertically aligned pores in freeze-cast cryogels, (e-I–III) macro-to-micro-scale scattering: (e-I) between the filaments, (e-II) between the interfacial skin and core, and (e-III) within the porous core. (f) A comparison of the SSE/t *vs.* density of fabricated GO-based cryogels. All error bars in (a)–(c) represent the standard deviation. The abbreviations DM, ET, CC, FC, and WL correspond to direct-molded, emulsion-templated, chemically-crosslinked, freeze-cast, and worm-like cryogels, respectively.

the material, offering a comprehensive understanding of the shielding mechanisms.[9,68]

Furthermore, the total EMI shielding effectiveness (SE_T) is determined by the logarithmic ratio of incident power to the transmitted power of the plane waves. As per Schelkunoff's theory, SE_T is calculated by taking three factors into consideration: EMI reflection effectiveness (SE_R), EMI absorption effectiveness (SE_A), and the shielding effectiveness resulting from multiple reflections (SE_M).[69,70] As a result, the higher SE_T value signifies the better ability of a material to block EMWs whether through reflection and absorption. It is imperative to emphasize that assessing the predominant shielding mechanisms should rely merely on power coefficients or their interrelations, *i.e.*, *R*, *A*, or *R*/*A*. Regrettably, some previous studies have incorrectly evaluated the basic EMI shielding properties of materials by comparing the ratio of SE_A and SE_R. This comparison of logarithmic ratios is a fundamentally flawed practice and results in misinterpretation of the shielding mechanisms.[22]

The EMI shielding characteristics of all cryogels with distinct morphologies are depicted in Fig. 5(b), (c) and the ESI† for the thickness range of 6.74–8.05 mm (Fig. S19–S23 and Table S1, ESI†). In general, higher electrical conductivity results in a reflection-dominant EMI shielding mechanism. This can be explained by the high impedance mismatch between the highly conductive structure and free space. It should be noted that impedance is the ratio of the transverse components of the

electric and magnetic fields of EMWs propagating through a medium, where lower impedance compared to free space signifies the ability of the structure to reflect EMWs.[71] In such scenarios, EMWs transfer their energy to the electrons and other charged particles within the shield, causing them to oscillate and generate a scattered electromagnetic field, which manifests as reflected waves. In this regard, the chemically-crosslinked cryogels with the highest electrical conductivity among all prepared samples reflected ~70% of the incident waves. However, this high reflectance is not ideal, as it creates secondary electromagnetic pollution, which is as detrimental as the original incident wave.

Apart from reflection, a portion of the EMWs penetrates the shield's body and is absorbed within its structure, dissipating EMWs' energy in the form of heat. This absorption mechanism occurs due to active electric/magnetic dipoles and materials with finite electrical conductivity in shields.[72] Absorption in cryogel-based EMI shields is directly influenced by multiple internal reflections or internal scattering, another paramount mechanism affecting their performance. In this scenario, shields with a multitude of mismatched impedance interfaces trap EMWs inside their body, prolonging the propagation path by multiple back-and-forth reflections within the shield. This elongated propagation path before transmission enhances the interactions between the shield and transmitted waves, leading to the dissipation of EMW energy.[22]

Elongated and complex pores can effectively extend the propagation path and enhance absorption, as illustrated in Fig. 5(d) and (e). Freeze-cast cryogels exemplify this principle, achieving an absorbance of ~55% through improved multiple internal reflections that guide waves through longer, vertically oriented pores. Similarly, worm-like cryogels, characterized by dual macro-to-micro-scale porosities and multiple interfaces, predominantly absorb the wave's energy. The energy of EMWs is attenuated due to internal scattering phenomena between filaments with mismatched impedance, dissipating within the enveloped porous core. This process of multiple internal reflection significantly enhances the absorption capacity, achieving a rate of 54.7% for worm-like cryogels. Among various cryogel types, worm-like and chemically-crosslinked cryogels exhibit the highest SE_T, ranging from 42.9 to 43.2 dB. However, it is crucial to distinguish between these cryogels' performances, as their shielding mechanisms differ significantly. Chemically-crosslinked cryogels primarily reflect a major portion of EMWs, while worm-like cryogels absorb most of EMWs through internal scattering across macro-to-micro-scale porosity. Despite having a nearly similar electrical conductivity range to worm-like cryogels, direct-molded cryogels achieve a lower SE_T of 27.5 dB due to their lower porosity. This underscores the importance of considering both structural characteristics and electrical conductivity in cryogels for EMI shielding. In this scenario, enhancing electrical conductivity may not lead to more efficient shields, as evidenced by the higher reflection rate. Indeed, the integration of fine-tuned porosity and effectively controlling electrical conductivity warrants the versatility of cryogels in efficient EMI shields.

To assess the impact of density and thickness—critical factors for EMI shields in advanced electronics—shielding effectiveness values are often normalized by these parameters. This normalization results in the specific EMI shielding effectiveness (SSE/t), offering a clearer understanding of the shielding capabilities. The SSE/t of the developed cryogels is compared with each other Fig. 5(f). Moreover, a comparison of thickness, electrical conductivity, density, SE_T, absorbance, and SSE/t of these cryogels is also outlined in Table S1 of the ESI.† The results demonstrate that worm-like cryogels, with lower density and higher SE_T values, significantly outperform other fabricated constructs in terms of SSE/t. This, along with the unique absorption-dominant behavior of these cryogels, underscores the liquid streaming approach as a method deserving further emphasis in future research.

Evaluating the EMI shielding performance of cryogels after being subjected to cyclic compressive loading is essential to assess their long-term performance. This testing simulates real-world conditions, where materials are exposed to repeated mechanical stresses, ensuring that the cryogel maintains its structure and functional properties over time. Post-compression, the overall thickness of the samples decreases due to cell wall and structural damage (Fig. S24a, ESI†). Likewise, the compressive loading induces fractures within the conductive network of the cryogel, thereby leading to a reduction in electrical condictivity (Fig. S24b, ESI†). This change in thickness and electrical conductivity directly impacts the shielding characteristics, as shown in Fig. S24c, d and S25–S29 (ESI†). The results indicate that the shielding mechanism of the chemically-crosslinked cryogels altered from reflection-dominant to absorption-dominant, achieving an absorption rate of ~59.9%. This shift can be attributed to the cracks and bumps on the highly conductive skin and within the cryogel's bulk, all caused by the cyclic compression test. Of note, despite showcasing absorption characteristics, the SE_T of these cryogels significantly reduces to 23.9 dB.

In the case of direct-molded and emulsion-templated cryogels, they retained their absorption behavior with high rates of ~71.1% and 62.1%, respectively. However, a noticeable reduction in SE_T was observed in these cryogel types compared to their original form before compression. This reduction occurs due to a decrease in electrical conductivity and physical changes in the cryogel's structure, such as compression-induced damage or alterations in porosity. These changes are further compounded by the absence of cell wall alignments or engineered structural designs, unlike the freeze-cast and worm-like cryogels. In this context, the compressed freeze-cast cryogels with directional aligned structure and worm-like cryogels with macro-to-micro-scale porosity not only preserved their absorption characteristics but also demonstrated a SE_T of ~37.9 and 33.4 dB, respectively. It is worth noting that the slight increase in shielding effectiveness of the compressed freeze-cast cryogels may be attributed to the densification of the cryogel's structure or better alignment of conductive pathways caused by cyclic compressive forces. This suggests that cyclic loading may have positively influenced the material's structure, enhancing rather than compromising the shielding

performance of freeze-cast cryogels. This makes them ideal for applications where mechanical resilience is coupled with effective EMI protection.

3. Conclusion

In this study, we developed GO-based cryogels using various fabrication methods, including molding, emulsion templating, chemically-induced gelation, unidirectional freeze-casting, and liquid-in-liquid streaming techniques. Upon thermal annealing, these porous constructs, with electrical conductivity ranging from 8.6 to 137.3 S m^{-1}, exhibited distinct shielding performance. For instance, chemically-crosslinked cryogels with the highest reported electrical conductivity among all prepared samples were reflection-dominant, exhibiting a high reflectance of $\sim$70% and a SE_T of 43.2 dB. In contrast, worm-like cryogels prepared through liquid streaming method using the same GO and thermal treatment conditions, showcased a similar SE_T of 42.9 dB but exhibited unique absorption-dominant EMI shielding mechanisms with an absorbance of 54.7%. Based on these findings, we recommend that future research focus simultaneously on both the internal structure and electrical conductivity of cryogel-based EMI shields, rather than solely prioritizing the electrical conductivity of the constructs, as is traditionally conducted in synthetic EMI shields.

4. Experimental section

4.1. Materials

For the synthesis of GO, highly concentrated sulfuric acid (H_2SO_4 95–98%), *ortho*-phosphoric acid (H_3PO_4, 85%), potassium permanganate ($KMnO_4$), hydrogen peroxide (H_2O_2, 30%), hydrochloric acid (HCl, 37%), and anhydrous ethanol (C_2H_6O, water content of $\leq$0.003%) were provided by Sigma-Aldrich. Graphite flakes were supplied by Asbury Carbons. Hexane (C_6H_{14}, 97%) and PSS-[3-(2-aminoethyl)amino]propyl-heptaisobutyl substituted POSS (POSS–NH_2), which were used for liquid-in-liquid streaming and emulsion templating, were provided by Sigma-Aldrich. For chemically-induced gelation, the gelation agent, ethylenediamine (EDA), was also supplied by Sigma-Aldrich. Ultra-pure deionized (DI) water with a resistivity of 18.2 MΩ (ELGA model MEDICA EDI 15/30) was used for all experiments.

4.2. Methods

4.2.1. Synthesis of graphene oxide. The synthesis of GO involves exfoliating graphite flakes through four essential phases: intercalation, oxidation, termination, and purification. The GO was synthesized using a modified adaptation of the Hummers' approach, as previously studied by Marcano *et al.*[73] Initially, a ratio of 9 : 1 (360 : 40 ml) mixture of H_2SO_4 : H_3PO_4 was stirred at 300 rpm for 10 min. Following this, 3 g of large flake graphite was added to the acidic mixture and stirred for 30 min at ambient temperature. The solution's temperature was reduced to 0–5 °C using an ice bath, and then 18 g of $KMnO_4$ was gradually added over 1 h. In the next stage, the temperature of the batch was raised to 50 °C and stirred continuously for 18 h. The process was then terminated by adding a mixture of 5 ml of H_2O_2 and 800 ml of deionized water.

The acquired solution underwent a step-wise purification protocol using DI water, 30 vol% HCl, and ethyl alcohol. The resulting purified mixture was carefully diluted to $\sim$2 mg ml^{-1} and exposed to low-power bath sonication for 30 min. Finally, the resulting suspension was centrifuged at 3500 rpm for 1 h to remove unreacted graphite and the few-layer graphite oxide flakes from the primary product. The isolated supernatant was centrifuged at 11 000 rpm for 1 h, forming a dense GO paste. The concentration was then adjusted to 10 mg ml^{-1}, and the resulting paste was stored in a sealed container.

4.2.2. Molded cryogels. The molded cryogels were produced by pouring $\sim$10 mg ml^{-1} of GO aqueous suspension into a polystyrene container. After a gentle bath sonication for 30 min on a low-power mode, the container was placed in an ultra-freezer and maintained at −80 °C for 24 h. Subsequently, the frozen samples were subjected to lyophilization for 48 h. Random ice crystal formation within the aqueous suspension followed by freeze-drying featured a disordered sponge-like 3D structure. Following a post-processing thermal reduction at 800 °C under argon for 1 h, the cryogel was transformed to reduced electrically conductive cryogels.

4.2.3. Emulsion-templated cryogels. Emulsion-templated cryogels were generated upon successive templating, freezing, and freeze-drying of GO–hexane/POSS–NH_2 emulsions. The structured emulsion was made by blending a 60 : 40 vol% ratio of $\sim$10 mg ml^{-1} GO aqueous suspension with a non-polar solution containing 1 mg ml^{-1} hexane/POSS–NH_2. The GO–hexane/POSS–NH_2 mixture was vigorously stirred for 5 min, ensuring effective emulsification and a homogeneous GO–hexane/POSS–NH_2 composition. The resulting structured emulsion was decanted into a transparent polystyrene container jar and then subjected to lyophilization and thermal reduction, similar to the process described in Section 4.2.2.

4.2.4. Chemically-crosslinked cryogels. To develop chemically-crosslinked cryogels, $\sim$10 mg ml^{-1} GO aqueous suspension was mixed with 50 μl of EDA. The resulting solution was stirred for 5 min, sealed in a glass vial, and heated at 95 °C for 6 h. During this stage, gelation occurred due to chemical cross-linking of GO nanosheets, forming reduced GO hydrogels with a hierarchical structure.[33] Subsequently, the resulting hydrogel was washed with DI water three times and subjected to the lyophilization and post-processing thermal reduction process as described in Section 4.2.2.

4.2.5. Freeze-cast directional cryogels. A cylindrical mold made of polylactic acid (PLA), with an inner diameter of 20 mm and a depth of 10 mm, was fabricated using a 3D printer (Pro2 Plus-Fused Deposition Modeling). The mold was lined with a layer of copper foil at the bottom. To establish a unidirectional freeze-casting setup, a copper table was immersed in a styrofoam tub filled with liquid nitrogen. The prepared mold containing 20 ml of $\sim$10 mg ml^{-1} GO aqueous suspension was then placed on the top of the copper table to achieve unidirectional freeze-cast samples. The controlled bottom-up ice crystal growth along the established temperature gradient played a templating role in aligning GO flakes and forming

compacted walls around the vertically aligned ice crystals. The oriented structures underwent lyophilization and thermal reduction, as detailed in Section 4.2.2.

4.2.6. Worm-like cryogels. To achieve worm-like structured liquids, we streamlined ~10 mg ml^{-1} GO aqueous mixture into a non-polar domain containing POSS–NH_2 ligands using a 3D bioprinter (Allevi 2). With a 200 μm injection needle, we set the extrusion pressure at 15–30 psi to ensure stable worm-like liquids. Upon injection, interfacial skin forms around the filament due to the electrostatic interaction between GO in the aqueous phase and the protonated ligand (POSS–NH_3^+) in the oil phase. This robust skin plays a crucial role in preventing the collapse of the aqueous jet into distinct droplets by suppressing Plateau-Rayleigh instabilities. Finally, the customized filamentous liquid templates underwent lyophilization and thermal reduction, as mentioned in Section 4.2.2., transforming the structured liquids into reduced worm-like cryogels with 3D morphologies and dual macro-to-micro porosity.

4.3. Characterization

The general characterizations of GO and cryogels made by various fabrication methods were conducted *via* various techniques. X-ray diffraction (XRD) (Brucker D8 Advance) was used the scattered X-rays were collected by an Eiger2R 500 K detector. Micro-Raman spectroscopy (Brucker Senterra II) equipped with an Olympus U-TV1X-2 microscope was employed to assess the D-band, G-band, and structural defects, *i.e.*, the ratio of I_D/I_G. Likewise, the Fourier-transform infrared spectroscopy (FTIR) (Nicolet-S20) within the range of 600–4000 cm^{-1} was employed to assess the functionality of GO.

The morphological assessments of the developed cryogels were conducted *via* a field emission scanning electron microscope (FESEM) (Tescan Mira 3 XMU). An Oxford Instruments X-Max energy dispersive spectrometer (EDS) detector was assembled on the FESEM to evaluate the elemental distribution of nanomaterials. The morphology and atomic structure of the GO flakes were assessed *via* high-resolution transmission electron microscopy (HRTEM) (80–300 Titan LB) equipped with an aberration-corrector (CEOS), operated at 300 kV; images were also acquired using a First Light CCD, Gatan. The confocal microscope imaging was conducted using the Leica DMi8 confocal microscope. For this purpose, the oil-in-water emulsion was stained with Calcofluor White Stain and then visualized by the confocal microscope.

Dynamic interfacial tension (IFT) tests of water and aquatic GO inks were carried out by holding a GO droplet within the hexane domain with/without POSS, using the DSA KRÜSS Scientific drop shape analyzer model DSA25E. The nanoparticle jamming was examined through the expansion/contraction of the pendant droplet by injecting a 1 mg ml^{-1} of GO aqueous suspension into the hexane/POSS medium. A universal tensile machine (Z010 Zwick/Roell) was used to evaluate the mechanical characteristics of cryogels to apply the cyclic compression tests at 20%, 40%, 60%, 70%, and 80% of compressive strains with a loading/unloading speed of 8 mm min^{-1}.

After thermal annealing at 800 °C under argon, the electrical conductivity of the cryogels was measured by a Loresta GP resistivity meter (Mitsubishi Chemical Co. model MCP-T700). The skin of the chemically-crosslinked cryogels was removed using a blade to facilitate a comparison of the electrical conductivity between these cryogels with/without skin.

The EMI shielding capability of conductive GO-based cryogels was evaluated within the X-band frequency range (8.2–12.4 GHz) using a two-port vector network analyzer (VNA) (P9374A Keysight) equipped with a WR-90 rectangular waveguide. The mechanism of VNA setup is discussed in Section S2.2, ESI.†

Data availability

All the experimental data of this manuscript and the ESI† are provided in the attached ESI† (including the excel file of raw data).

Conflicts of interest

There are no conflicts to declare.

Acknowledgements

The authors acknowledge the Syilx Okanagan Nation for the use of their traditional, ancestral, and unceded territory, the land on which the research was conducted. The authors acknowledge the support of the Natural Sciences and Engineering Research Council of Canada (NSERC) [funding reference numbers ALLRP 555586-20 and RGPIN-2020-03914]. M. A. would like to express appreciation for the financial support provided by the Canada Research Chairs Program. We are grateful for the kind support of the Fipke Laboratory for Trace Element Research (FiLTER) for granting us access to their FESEM.

References

1 H. Wang, S. Li, M. Liu, J. Li and X. Zhou, *Macromol. Mater. Eng.*, 2021, **306**, 2100032.
2 X.-X. Wang, Q. Zheng, Y.-J. Zheng and M.-S. Cao, *Carbon*, 2023, **206**, 124–141.
3 J.-M. Thomassin, C. Jérôme, T. Pardoen, C. Bailly, I. Huynen and C. Detrembleur, *Mater. Sci. Eng., R*, 2013, **74**, 211–232.
4 X.-X. Wang, J.-C. Shu, W.-Q. Cao, M. Zhang, J. Yuan and M.-S. Cao, *Chem. Eng. J.*, 2019, **369**, 1068–1077.
5 R. Kumar, S. Sahoo, E. Joanni and J.-J. Shim, *Composites, Part B*, 2023, 110874.
6 R. Kumar, S. Sahoo, E. Joanni, R. K. Singh, W. K. Tan, S. A. Moshkalev, A. Matsuda and K. K. Kar, *Crit. Rev. Solid State Mater. Sci.*, 2022, **47**, 570–619.
7 A. Ghaffarkhah, S. A. Hashemi, F. Ahmadijokani, M. Goodarzi, H. Riazi, S. E. Mhatre, O. Zaremba, O. J. Rojas, M. Soroush and T. P. Russell, *Nat. Commun.*, 2023, **14**, 7811.
8 S. Geetha, K. Satheesh Kumar, C. R. Rao, M. Vijayan and D. Trivedi, *J. Appl. Polym. Sci.*, 2009, **112**, 2073–2086.

9 S. B. Kondawar and P. R. Modak, *Materials for Potential EMI Shielding Applications*, Elsevier, 2020, pp. 9–25.
10 A. Ghaffarkhah, S. A. Hashemi, S. Rostami, M. Amini, F. Ahmadijokani, A. Pournaghshband Isfahani, S. E. Mhatre, O. J. Rojas, M. Kamkar and S. Wuttke, *Adv. Funct. Mater.*, 2023, **33**, 2304748.
11 N. Bagotia, V. Choudhary and D. Sharma, *Polym. Adv. Technol.*, 2018, **29**, 1547–1567.
12 D. X. Yan, H. Pang, B. Li, R. Vajtai, L. Xu, P. G. Ren, J. H. Wang and Z. M. Li, *Adv. Funct. Mater.*, 2015, **25**, 559–566.
13 T. Blachowicz, G. Ehrmann and A. Ehrmann, *Macromol. Mater. Eng.*, 2023, 2200692.
14 Y. Wang and X. Jing, *Polym. Adv. Technol.*, 2005, **16**, 344–351.
15 P. J. Bora, A. G. Anil, K. J. Vinoy and P. C. Ramamurthy, *Adv. Mater. Interfaces*, 2019, **6**, 1901353.
16 S. H. Kim, S. H. Jang, S. W. Byun, J. Y. Lee, J. S. Joo, S. H. Jeong and M. J. Park, *J. Appl. Polym. Sci.*, 2003, **87**, 1969–1974.
17 T. Mäkelä, S. Pienimaa, T. Taka, S. Jussila and H. Isotalo, *Synth. Met.*, 1997, **85**, 1335–1336.
18 Y. Wang, F.-q Gu, L.-j Ni, K. Liang, K. Marcus, S.-l Liu, F. Yang, J.-j Chen and Z.-s Feng, *Nanoscale*, 2017, **9**, 18318–18325.
19 R. Cheng, B. Wang, J. Zeng, J. Li, J. Xu, W. Gao and K. Chen, *Carbon*, 2023, **202**, 314–324.
20 Z. Guo, P. Ren, J. Wang, J. Tang, F. Zhang, Z. Zong, Z. Chen, Y. Jin and F. Ren, *Composites, Part B*, 2022, **236**, 109836.
21 Y.-Y. Wang, F. Zhang, N. Li, J.-F. Shi, L.-C. Jia, D.-X. Yan and Z.-M. Li, *Carbon*, 2023, **205**, 10–26.
22 A. A. Isari, A. Ghaffarkhah, S. A. Hashemi, S. Wuttke and M. Arjmand, *Adv. Mater.*, 2024, 2310683.
23 X. C. Tong, *Advanced Materials and Design for Electromagnetic Interference Shielding*, CRC Press, 2016.
24 F. Shahzad, M. Alhabeb, C. B. Hatter, B. Anasori, S. Man Hong, C. M. Koo and Y. Gogotsi, *Science*, 2016, **353**, 1137–1140.
25 T. Yun, H. Kim, A. Iqbal, Y. S. Cho, G. S. Lee, M. K. Kim, S. J. Kim, D. Kim, Y. Gogotsi and S. O. Kim, *Adv. Mater.*, 2020, **32**, 1906769.
26 Z. Cheng, R. Wang, Y. Wang, Y. Cao, Y. Shen, Y. Huang and Y. Chen, *Carbon*, 2023, **205**, 112–137.
27 Y. Chen, Y. Yang, Y. Xiong, L. Zhang, W. Xu, G. Duan, C. Mei, S. Jiang, Z. Rui and K. Zhang, *Nano Today*, 2021, **38**, 101204.
28 K. Tian, D. Hu, Q. Wei, Q. Fu and H. Deng, *J. Mater. Sci. Technol.*, 2023, **134**, 106–131.
29 Y. Cao, Z. Cheng, R. Wang, X. Liu, T. Zhang, F. Fan and Y. Huang, *Carbon*, 2022, **199**, 333–346.
30 Z. Cheng, Y. Cao, R. Wang, X. Liu, F. Fan and Y. Huang, *J. Mater. Chem. A*, 2023, **11**, 5593–5605.
31 L. Ma, M. Hamidinejad, L. Wei, B. Zhao and C. B. Park, *Mater. Today Phys.*, 2023, **30**, 100940.
32 M.-S. Cao, J.-C. Shu, B. Wen, X.-X. Wang and W.-Q. Cao, *Small Struct.*, 2021, **2**, 2100104.
33 H. Hu, Z. Zhao, W. Wan, Y. Gogotsi and J. Qiu, *Adv. Mater.*, 2013, **25**, 2219–2223.
34 S. Rostami, A. Ghaffarkhah, A. Isari, S. A. Hashemi and M. Arjmand, *Mater. Adv.*, 2023, 2698–2729.
35 G. Shao, D. A. Hanaor, X. Shen and A. Gurlo, *Adv. Mater.*, 2020, **32**, 1907176.
36 H. Zhang, *Ice Templating and Freeze-drying for Porous Materials and Their Applications*, John Wiley & Sons, 2018.
37 S. Deville, *J. Mater. Res.*, 2013, **28**, 2202–2219.
38 N. A. Pohan, M. H. Wahid, Z. Zainal and N. A. Ibrahim, *RSC Adv.*, 2021, **11**, 3963–3971.
39 R. Menzel, S. Barg, M. Miranda, D. B. Anthony, S. M. Bawaked, M. Mokhtar, S. A. Al-Thabaiti, S. N. Basahel, E. Saiz and M. S. Shaffer, *Adv. Funct. Mater.*, 2015, **25**, 28–35.
40 W. Zhang, Q. Q. Kong, Z. Tao, J. Wei, L. Xie, X. Cui and C. M. Chen, *Adv. Mater. Interfaces*, 2019, **6**, 1900147.
41 Z. Yu, M. McInnis, J. Calderon, S. Seal, L. Zhai and J. Thomas, *Nano Energy*, 2015, **11**, 611–620.
42 S. A. Hashemi, A. Ghaffarkhah, M. Goodarzi, A. Nazemi, G. Banvillet, A. S. Milani, M. Soroush, O. J. Rojas, S. Ramakrishna and S. Wuttke, *Adv. Mater.*, 2023, **35**, 2302826.
43 S. S. Kistler, *Nature*, 1931, **127**, 741.
44 S. S. Kistler, *J. Phys. Chem.*, 2002, **36**, 52–64.
45 G. Gorgolis and C. Galiotis, *2D Mater.*, 2017, **4**, 032001.
46 Y. Li, W. Wei, Y. Wang, N. Kadhim, Y. Mei and Z. Zhou, *J. Mater. Chem. C*, 2019, **7**, 11783–11789.
47 G. Nassar, E. Daou, R. Najjar, M. Bassil and R. Habchi, *Carbon Trends*, 2021, **4**, 100065.
48 Y. Yang, Z. Xia, Y. Luo, Z. Wu, S. Shi and T. P. Russell, *Supramol. Mater.*, 2022, **1**, 100013.
49 M. Kamkar, A. Ghaffarkhah, R. Ajdary, Y. Lu, F. Ahmadijokani, S. E. Mhatre, E. Erfanian, U. Sundararaj, M. Arjmand and O. J. Rojas, *Small*, 2022, **18**, 2200220.
50 M. Kamkar, E. Erfanian, P. Bazazi, A. Ghaffarkhah, F. Sharif, G. Xie, A. Kannan, M. Arjmand, S. H. Hejazi and T. P. Russell, *Adv. Mater. Interfaces*, 2022, **9**, 2101659.
51 Z. Sun, T. Feng and T. P. Russell, *Langmuir*, 2013, **29**, 13407–13413.
52 A. Toor, T. Feng and T. P. Russell, *Eur. Phys. J. E: Soft Matter Biol. Phys.*, 2016, **39**, 1–13.
53 S. Shi and T. P. Russell, *Adv. Mater.*, 2018, **30**, 1800714.
54 S. Shi, B. Qian, X. Wu, H. Sun, H. Wang, H. B. Zhang, Z. Z. Yu and T. P. Russell, *Angew. Chem., Int. Ed.*, 2019, **58**, 18171–18176.
55 I. Covarrubias-García, G. Quijano, A. Aizpuru, J. L. Sánchez-García, J. L. Rodríguez-López and S. Arriaga, *J. Hazard. Mater.*, 2020, **397**, 122760.
56 C.-B. Li, Y.-J. Li, Q. Zhao, Y. Luo, G.-Y. Yang, Y. Hu and J.-J. Jiang, *ACS Appl. Mater. Interfaces*, 2020, **12**, 30686–30694.
57 Q. Zhang, X. Xu, H. Li, G. Xiong, H. Hu and T. S. Fisher, *Carbon*, 2015, **93**, 659–670.
58 X. Xu, H. Li, Q. Zhang, H. Hu, Z. Zhao, J. Li, J. Li, Y. Qiao and Y. Gogotsi, *ACS Nano*, 2015, **9**, 3969–3977.
59 M. Pimenta, G. Dresselhaus, M. S. Dresselhaus, L. Cancado, A. Jorio and R. Saito, *Phys. Chem. Chem. Phys.*, 2007, **9**, 1276–1290.
60 K. K. H. De Silva, P. Viswanath, V. K. Rao, S. Suzuki and M. Yoshimura, *J. Phys. Chem. C*, 2021, **125**, 7791–7798.

61 A. C. Pierre and G. M. Pajonk, *Chem. Rev.*, 2002, **102**, 4243–4266.
62 H. Gesser and P. Goswami, *Chem. Rev.*, 1989, **89**, 765–788.
63 A. Borrás, G. Gonçalves, G. Marbán, S. Sandoval, S. Pinto, P. A. Marques, J. Fraile, G. Tobias, A. M. López-Periago and C. Domingo, *Chem. – Eur. J.*, 2018, **24**, 15903–15911.
64 Y. Cheng, S. Zhou, P. Hu, G. Zhao, Y. Li, X. Zhang and W. Han, *Sci. Rep.*, 2017, **7**, 1439.
65 C. Zhu, T. Y.-J. Han, E. B. Duoss, A. M. Golobic, J. D. Kuntz, C. M. Spadaccini and M. A. Worsley, *Nat. Commun.*, 2015, **6**, 6962.
66 M. Šilhavík, P. Kumar, Z. A. Zafar, M. Míšek, M. Čičala, M. Piliarik and J. Červenka, *Commun. Phys.*, 2022, **5**, 27.
67 D. Chung, *Mater. Chem. Phys.*, 2020, **255**, 123587.
68 M. Peng and F. Qin, *J. Appl. Phys.*, 2021, **130**, 225108.
69 S. A. Schelkunoff, *Bell Syst. Tech. J.*, 1943, **22**, 80–107.
70 S. Gupta and N.-H. Tai, *Carbon*, 2019, **152**, 159–187.
71 J. Wang, Q. Li, K. Li, X. Sun, Y. Wang, T. Zhuang, J. Yan and H. Wang, *Adv. Mater.*, 2022, **34**, 2109904.
72 M. Aswathi, A. V. Rane, A. Ajitha, S. Thomas and M. Jaroszewski, *Advanced Materials for Electromagnetic Shielding: Fundamentals, Properties, and Applications*, 2018, pp. 1–9.
73 D. C. Marcano, D. V. Kosynkin, J. M. Berlin, A. Sinitskii, Z. Sun, A. Slesarev, L. B. Alemany, W. Lu and J. M. Tour, *ACS Nano*, 2010, **4**, 4806–4814.